



OPEN ACCESS

EDITED BY

Cong Zhou,
East China University of Technology,
China

REVIEWED BY

Xiaoyue Cao,
Yangtze University, China
Ying Liu,
Ocean University of China, China
Bin Xiong,
Guilin University of Technology, China

*CORRESPONDENCE

Ya Sun,
✉ sunya_seis@csu.edu.cn

RECEIVED 09 March 2023

ACCEPTED 19 April 2023

PUBLISHED 15 June 2023

CITATION

Tong X, Sun Y and Zhang B (2023), An efficient spectral element method for two-dimensional magnetotelluric modeling. *Front. Earth Sci.* 11:1183150. doi: 10.3389/feart.2023.1183150

COPYRIGHT

© 2023 Tong, Sun and Zhang. This is an open-access article distributed under the terms of the [Creative Commons Attribution License \(CC BY\)](https://creativecommons.org/licenses/by/4.0/). The use, distribution or reproduction in other forums is permitted, provided the original author(s) and the copyright owner(s) are credited and that the original publication in this journal is cited, in accordance with accepted academic practice. No use, distribution or reproduction is permitted which does not comply with these terms.

An efficient spectral element method for two-dimensional magnetotelluric modeling

Xiaozhong Tong^{1,2}, Ya Sun^{1,2*} and Boyao Zhang¹

¹School of Geosciences and Info-Physics, Central South University, Changsha, China, ²Key Laboratory of Metallogenic Prediction of Nonferrous Metals of Ministry of Education, Central South University, Changsha, China

We introduce a new efficient spectral element approach to solve the two-dimensional magnetotelluric forward problem based on Gauss–Lobatto–Legendre polynomials. It combines the high accuracy of the spectral technique and the perfect flexibility of the finite element approach, which can significantly improve the calculation accuracy. This method mainly includes two steps: 1) transforming the boundary value problem in the partial differential form into the variational problem in the integral form and 2) solving large symmetric sparse systems based on the combination of incomplete LU factorization and the double conjugate gradient stability algorithm through the spectral element with quadrilateral meshes. We apply the spectral element method on a resistivity half-space model to obtain a simple analytical solution and find that the magnetic field solutions simulated by the spectral element approach matched closely to the exact solutions. The experiment result shows that the spectral element solution has high accuracy with coarse meshes. We further compare the numerical results of the spectral element, finite difference, and finite element approaches on the COMMEMI 2D-1 and smooth models, respectively. The numerical results of the spectral element procedure are highly consistent with the other two techniques. All these comparison results suggest that the spectral element technique can not only give high accuracy for modeling results but also provide more detailed information. In particular, a few nodes are required in this method relative to the finite difference and finite element methods, which can decrease the relative errors. We then deduce that the spectral element method might be an alternative approach to simulate the magnetotelluric responses in two- or three-dimensional structures.

KEYWORDS

magnetotelluric, two-dimensional, forward modeling, spectral element method, numerical experiments

1 Introduction

As a special geo-electromagnetic method, magnetotelluric sounding can identify the resistivity or conductivity distributions in a geological medium based on harmonic and variable electromagnetic fields (Chave and Jones, 2012). Magnetotelluric sounding is based on naturally occurring electromagnetic fields, which can provide a comprehensive and continuous spectrum of the geo-electromagnetic field. This electrical resistivity, measured by comparing the electric field's horizontal component to the magnetic field on the surface, can detect a depth of several tens of kilometers associated with the acquisition frequency. With the rapid advancement in magnetotelluric modeling and inversion, it has become one of the

essential tools for recognizing deep geological structures (Unsworth, 2010; Avdeeva et al., 2012; Azeez et al., 2017; Nagarjuna et al., 2021) and geophysical investigations, such as geothermal exploration (Barcelona et al., 2013; Patro, 2017; Tarek et al., 2023), mineral deposit exploration (Benjamin et al., 2018; Jiang et al., 2022), and gas exploration (Zhang et al., 2014).

There are some numerical approaches for solving two-dimensional magnetotelluric forward problems, such as finite difference and finite element, and they are applied to two-dimensional magnetotelluric inversion (deGroot-Hedlin and Constable, 1990; Rodi and Mackie, 2001; Siripunvaraporn and Egbert, 2007; Lee et al., 2009; Kelbert et al., 2014; Guo et al., 2020; Liao et al., 2022). The finite difference numerical approach can solve partial differential equations for approximating first-order or second-order derivatives with a difference scheme (Pek and Verner, 1997; deGroot-Hedlin, 2006; Rao and Babu, 2006; Kumar et al., 2011). They also investigated the efficiency of computing two-dimensional magnetotelluric responses. This method also has high accuracy on the electric field and magnetic field components (Guo et al., 2018; Kalscheuer et al., 2018; Sarakorn and Vachiratiengchai, 2018). Unfortunately, it is not easy to compute the resulting fields' accurate apparent resistivities and phases. As another important numerical approach, finite element can be applied to solve the two-dimensional magnetotelluric forward problem (Wannamaker et al., 1986; Key and Weiss, 2006; Franke et al., 2007; Lee et al., 2009; Sarakorn, 2017; Yao et al., 2021). It involves the hypothetical functional form of the model and the field in a small area of the specified geometry. The finite element method can introduce complex information from the real world to construct the initial model, including surface topography, and can also improve the flexibility of mesh discretization. However, it requires fine meshing to obtain high accuracy, which results in high computational costs. Some other numerical methods are also used to simulate two-dimensional magnetotelluric forward modeling, such as the boundary element (Xu and Zhou, 1997), the finite-volume (Du et al., 2016; Wang et al., 2019), the mesh-free (Wittke and Tezkan, 2014; Wittke and Tezkan, 2021), the domain decomposition (Bihlo et al., 2017), the numerical manifold (Liang et al., 2021), and the pseudo-spectral methods (Tong et al., 2020). These numerical methods provide an essential practical basis for two-dimensional magnetotelluric forward modeling.

Compared to other numerical approaches, the finite element method requires fine grids to obtain higher calculation accuracy. This will bring challenges, especially when computational resources are limited. Moreover, in practical geophysical applications, when the discrete meshes need to be refined to a geo-electrical model, the convergence rate will decrease gradually, while the number of meshes and the computational cost can increase largely (Key and Weiss, 2006). The spectral method, as a novel approach, can provide the numerical approximation of partial differential equations (Zou and Cheng, 2018). In this numerical approach, the field in the computational domain can be approximated by polynomials or Fourier expansions. Since high-order orthogonal basis functions are applied in the spectral method, it has exponential convergence. In addition, the spectral interpolation points are densely distributed at the boundary, which can avoid the Runge phenomenon in the traditional high-order interpolation (Tong et al., 2020). The method that combines the finite element and spectral method is called the

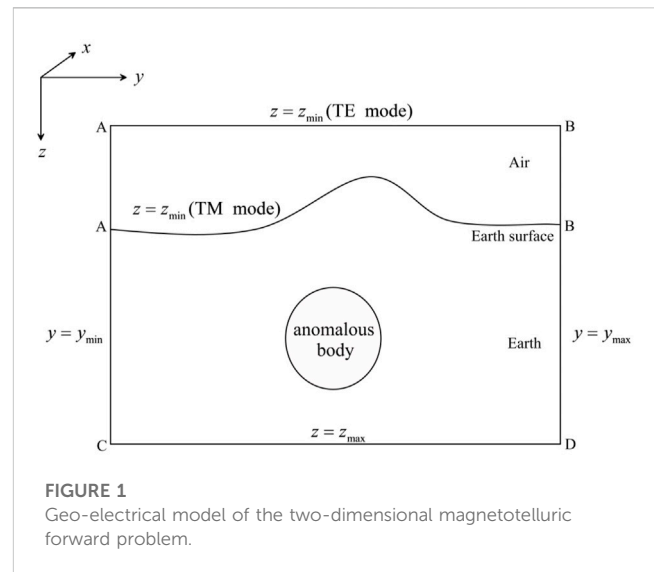


FIGURE 1
Geo-electrical model of the two-dimensional magnetotelluric forward problem.

spectral element method. In the past 20 years, geophysicists have dedicated these numerical methods to developing efficiency and accuracy. Some recent developments found that the spectral element approach can be seen as a high-order finite element method and its high-accuracy is derived from the properties of the spectral method (Patera, 1984). It can combine the high-accuracy of the spectral method and the flexibility of the finite element technique. Compared with the classical finite element method, the Runge phenomenon of isometric interpolation can be avoided using Gaussian orthogonal basis functions and Gaussian points (Xu et al., 2022). There are two types of spectral element methods, one based on Legendre polynomials and another based on Chebyshev polynomials. It is widely used in applications for wave propagation (Komatitsch and Tromp, 1999; Seriani and Oliveria, 2008; Luo et al., 2013; Trinh et al., 2019; Lyu et al., 2020), forward gravity modeling (Ghariti et al., 2018; Martin et al., 2017), and for geo-electromagnetic forward modeling problems (Zhou et al., 2016; Huang et al., 2019; Yin et al., 2019; Zhu et al., 2020; Huang et al., 2021; Weiss et al., 2023). However, it is rarely used in two-dimensional magnetotelluric forward modeling.

This paper proposes an efficient and accurate spectral element approach to compute the two-dimensional magnetotelluric responses of the boundary problem without measuring Earth's curvature. To benchmark the accuracy, we compare the numerical results of the spectral element forward algorithm with the analytical solutions and numerical results of the finite difference and finite element schemes. Although our approach can be applied to any two-dimensional geo-electromagnetic forward modeling, in this study, we demonstrate its implementation mainly in numerical experiments.

2 Boundary value problem

2.1 Electromagnetic equations

We define the z -axis at the depth and the x -axis along the geologic strike, as shown in Figure 1. Using a time-harmonic factor

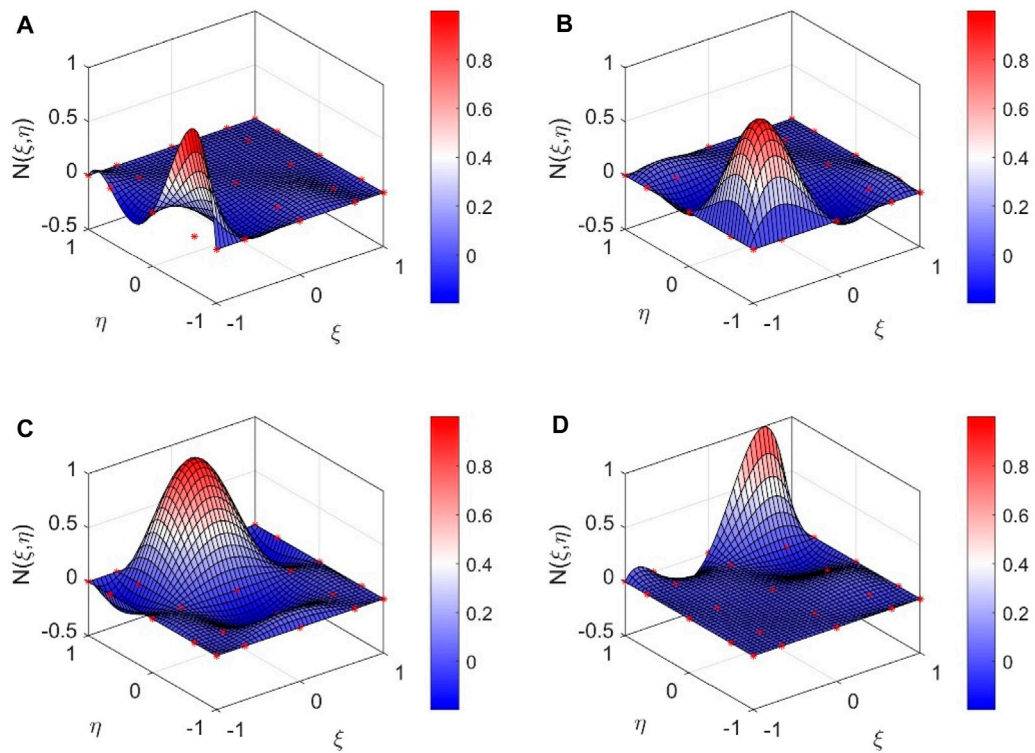


FIGURE 2 Two-dimensional spectral basis functions in part of order $p=4$. (A) $N_{12}(\xi, \eta) = \phi_1(\xi)\phi_2(\eta)$; (B) $N_{22}(\xi, \eta) = \phi_2(\xi)\phi_2(\eta)$; (C) $N_{34}(\xi, \eta) = \phi_3(\xi)\phi_4(\eta)$; and (D) $N_{45}(\xi, \eta) = \phi_4(\xi)\phi_5(\eta)$.

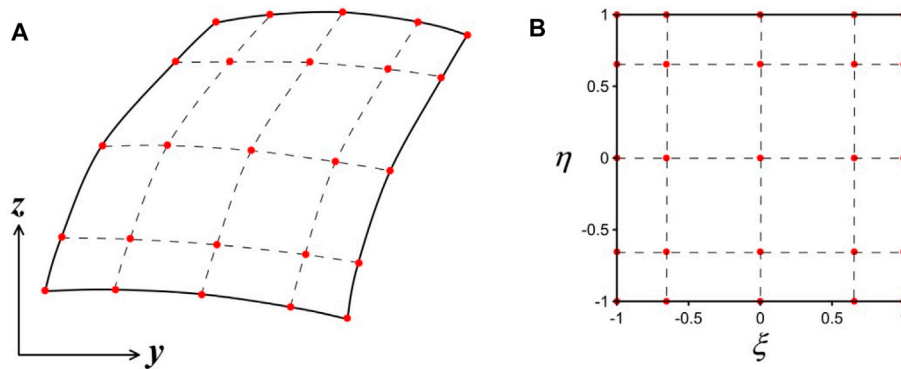


FIGURE 3 Mapping coordinate system of the spectral element of order $p = 4$. (A) Sub-element; (B) parent element.

$e^{-i\omega t}$, Maxwell's equations can then be written as (Wannamaker et al., 1987; Yao et al., 2021)

$$\nabla \times \mathbf{E} = i\omega\mu\mathbf{H} \tag{1}$$

$$\nabla \times \mathbf{H} = \sigma\mathbf{E} \tag{2}$$

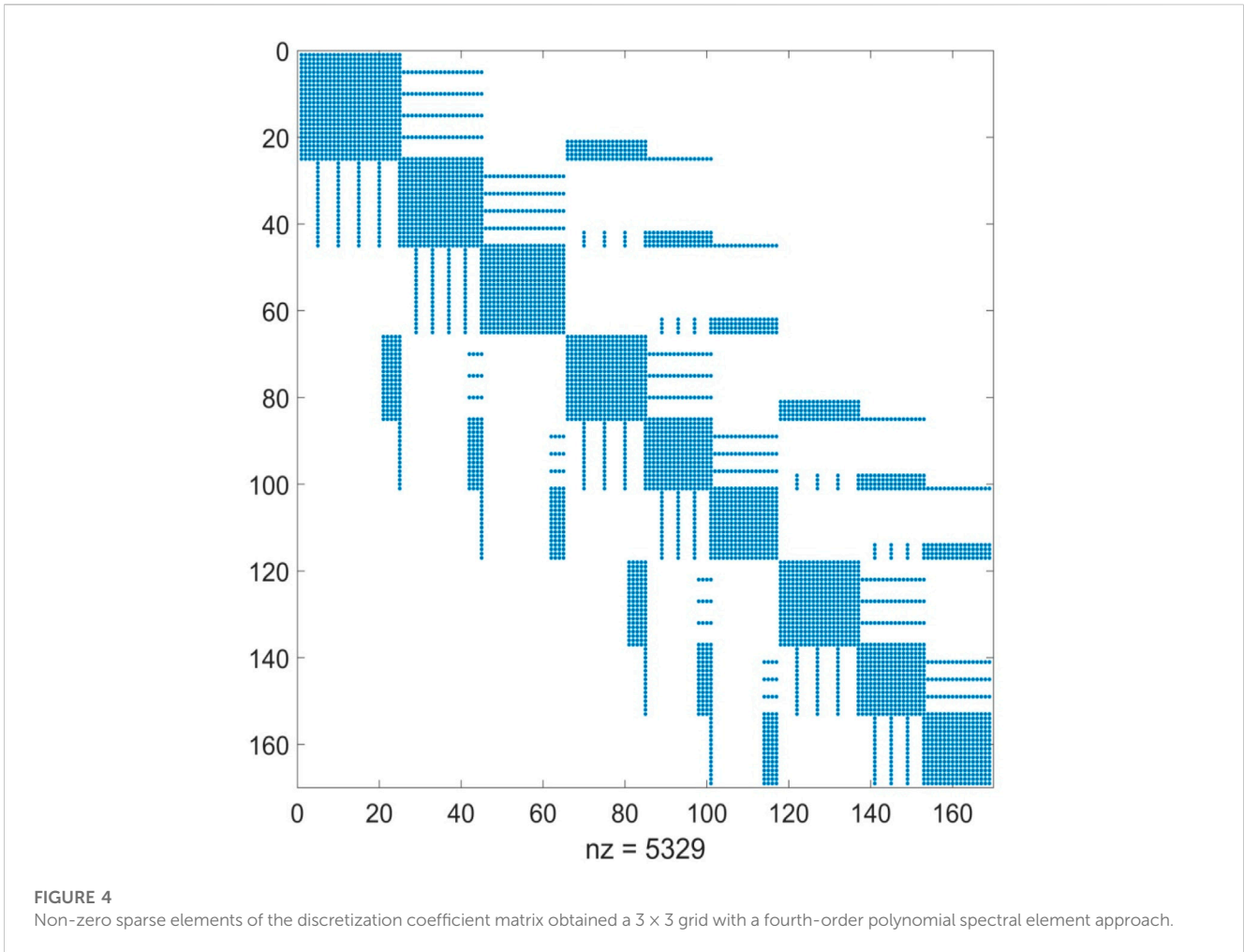
where \mathbf{E} means the electric field, \mathbf{H} represents the magnetic field, ω denotes the angular frequency, $\mu = 4\pi \times 10^{-7}\text{H/m}$ is the magnetic permeability, and σ is the conductivity.

For a two-dimensional structure, due to $\partial\mathbf{E}/\partial x \equiv 0$ and $\partial\mathbf{H}/\partial x \equiv 0$, we can expand the curl operators in Eqs 1, 2 as follows:

$$\frac{\partial E_z}{\partial y} - \frac{\partial E_y}{\partial z} = i\omega\mu H_x \tag{3}$$

$$\frac{\partial E_x}{\partial z} = i\omega\mu H_y \tag{4}$$

$$\frac{\partial E_x}{\partial y} = -i\omega\mu H_z \tag{5}$$



and

$$\frac{\partial H_z}{\partial y} - \frac{\partial H_y}{\partial z} = \sigma E_x \tag{6}$$

$$\frac{\partial H_x}{\partial z} = \sigma E_y \tag{7}$$

$$\frac{\partial H_x}{\partial y} = -\sigma E_z \tag{8}$$

The electromagnetic equations are more complex than homogeneous media for two-dimensional modeling, where resistivity changes occur in the y -axis and z -axis. According to Eqs 4–6, E_x the TE mode can yield a second-order Helmholtz equation:

$$\frac{\partial^2 E_x}{\partial y^2} + \frac{\partial^2 E_x}{\partial z^2} + i\omega\mu\sigma E_x = 0 \tag{9}$$

Meanwhile, for the TM mode, H_x yields another second-order Helmholtz equation:

$$\frac{\partial}{\partial y} \left(\frac{1}{\sigma} \frac{\partial H_x}{\partial y} \right) + \frac{\partial}{\partial z} \left(\frac{1}{\sigma} \frac{\partial H_x}{\partial z} \right) + i\omega\mu H_x = 0 \tag{10}$$

Then the electric field E_x or the magnetic field H_x in the Helmholtz-type equation can be rewritten as

$$\nabla \cdot (\tau \nabla u) + \lambda u = 0 \tag{11}$$

where u , τ , and λ represent different meanings relying on the different polarized modes. In the TE mode,

$$u = E_x, \tau = \frac{1}{i\omega\mu}, \lambda = \sigma \tag{12}$$

and in the TM mode,

$$u = H_x, \tau = \frac{1}{\sigma}, \lambda = i\omega\mu \tag{13}$$

2.2 Boundary conditions

We restrict the computational region for Eq. 11 to a two-dimensional bounded domain $\Omega = [y_{\min}, y_{\max}] \times [z_{\min}, z_{\max}]$, as shown in Figure 1. Therefore, the boundary conditions in the computational domain can be expressed as

$$u|_{z=z_{\min}} = 1 \text{ (in AB)} \tag{14a}$$

$$\frac{\partial u}{\partial y} \Big|_{y=y_{\min}} = 0 \text{ (in AC)}, \frac{\partial u}{\partial y} \Big|_{y=y_{\max}} = 0 \text{ (in BD)} \tag{14b}$$

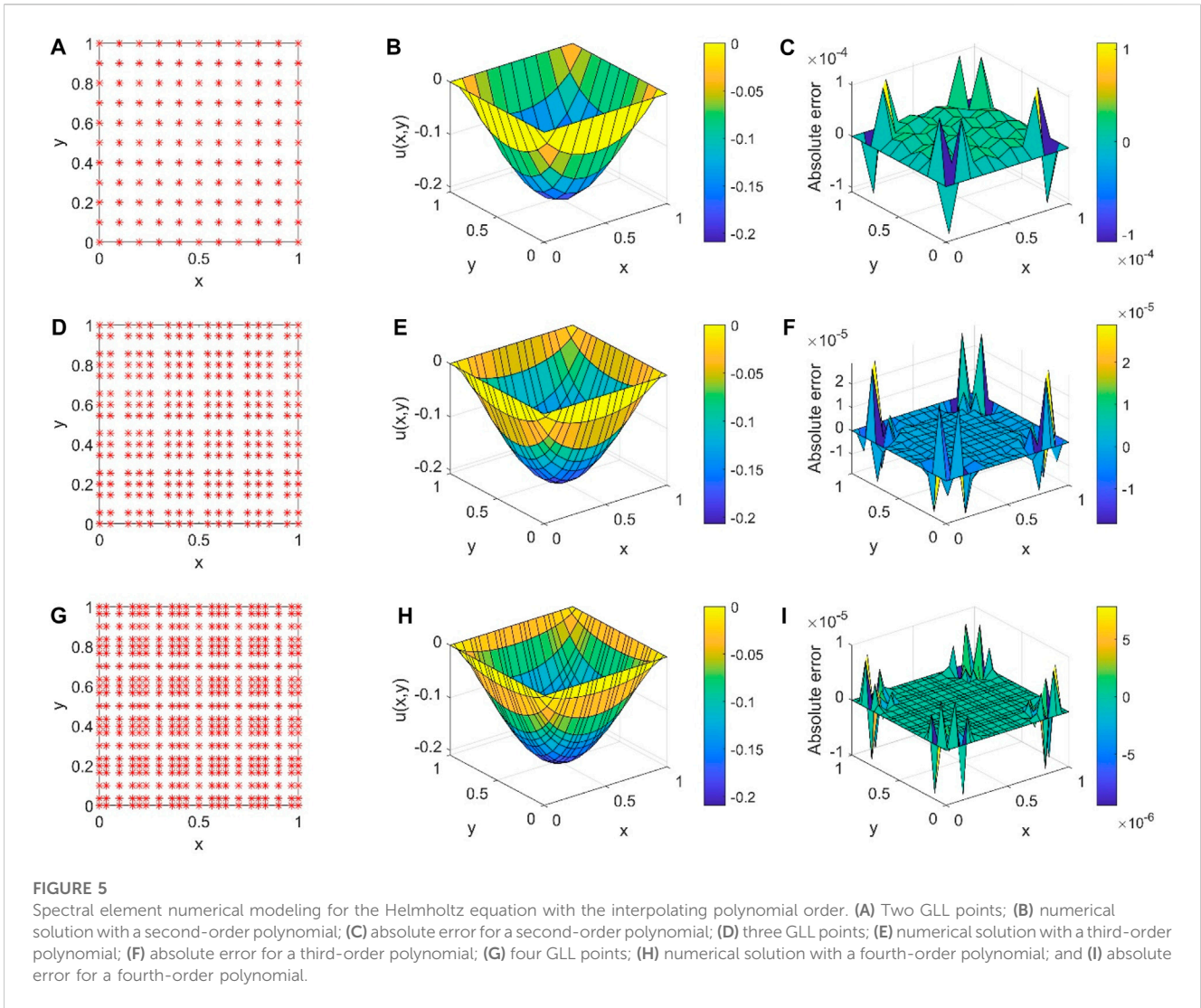


FIGURE 5

Spectral element numerical modeling for the Helmholtz equation with the interpolating polynomial order. (A) Two GLL points; (B) numerical solution with a second-order polynomial; (C) absolute error for a second-order polynomial; (D) three GLL points; (E) numerical solution with a third-order polynomial; (F) absolute error for a third-order polynomial; (G) four GLL points; (H) numerical solution with a fourth-order polynomial; and (I) absolute error for a fourth-order polynomial.

$$\left. \left(\frac{\partial u}{\partial z} + ku \right) \right|_{z=z_{\max}} = 0 \text{ (in CD)} \tag{14c}$$

where $k = \sqrt{-i\omega\mu\sigma}$.

3 Spectral element formulation

3.1 Discretization of a variational problem

The magnetotelluric fields can be simulated by the Helmholtz equation of Eq. 12 under the boundary conditions of Eq. 14. Using the variational principle (Pozrikidis, 2014), the boundary value problem of the partial differential form displayed in Eq. 12 and Eq. 14 can be written as the variational problem of the integral form:

$$\begin{cases} F(u) = \iint \left\{ \frac{1}{2} \tau \left[\left(\frac{\partial u}{\partial y} \right)^2 + \left(\frac{\partial u}{\partial z} \right)^2 \right] - \frac{1}{2} \lambda u^2 \right\} dydz + \int_{CD} \frac{1}{2} \tau k u^2 dl = \min \\ u|_{y=y_{\min}} = 0. \end{cases} \tag{15}$$

Within spectral element approximation, the magnetotelluric field can be expanded with two-dimensional interpolation basis functions:

$$\mathbf{u} = \sum_{i=1}^{N_r} N_i(\xi, \eta) u_i \tag{16}$$

where N_r is the number of primary procedures for an element and $N_i(\xi, \eta)$ are the essential functions.

The integral of all elements, Eq. 15, can be rewritten as

$$\begin{aligned} F(u) = \sum \iint_e \left\{ \frac{1}{2} \tau \left[\left(\frac{\partial u}{\partial y} \right)^2 + \left(\frac{\partial u}{\partial z} \right)^2 \right] - \frac{1}{2} \lambda u^2 \right\} dydz \\ + \sum \int_{CD} \frac{1}{2} \tau k u^2 dl = \min \end{aligned} \tag{17}$$

This will lead to a discrete linear equation as follows:

$$\mathbf{K} \mathbf{u} = 0 \tag{18}$$

where u represents the values of the unknown magnetic field or electric field.

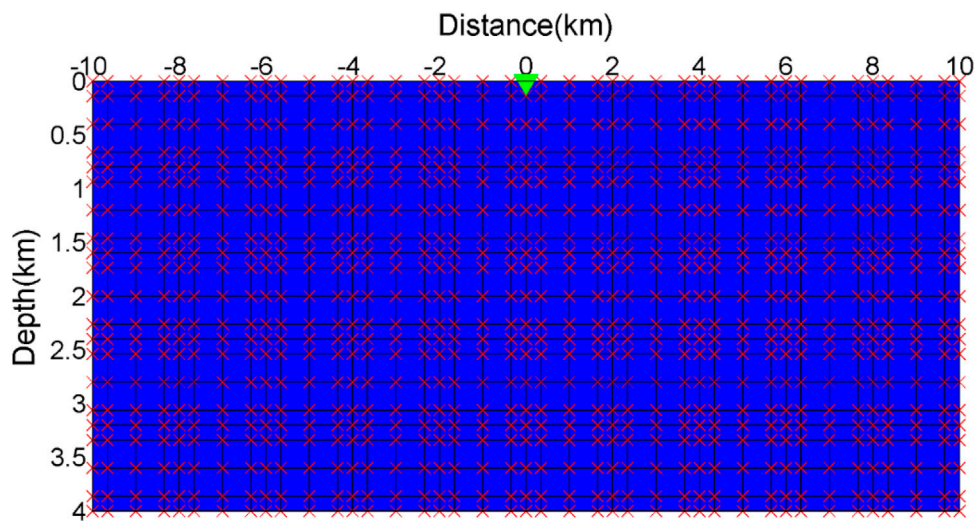


FIGURE 6
Homogeneous half-space model meshed with four GCL points per element.

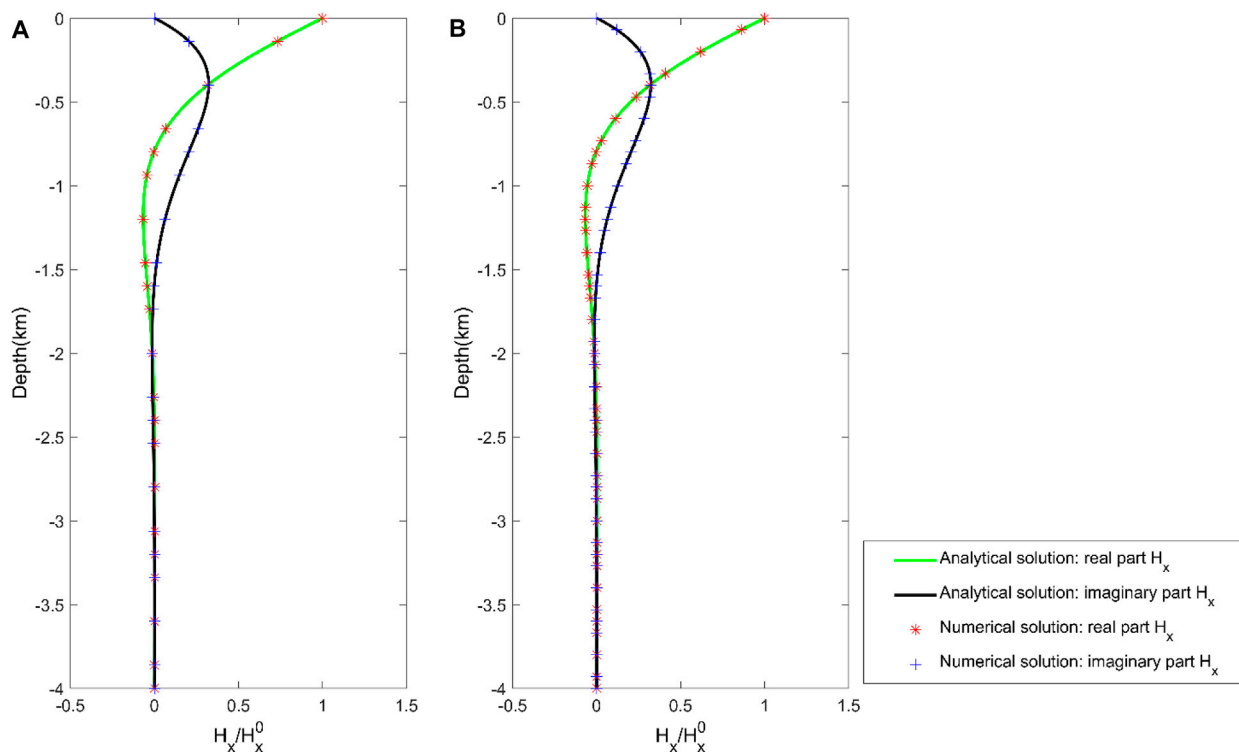


FIGURE 7
Spectral element numerical solution of magnetic field H_x for the frequency $f=10$ Hz in the half-space resistivity model. The number of elements in the depth direction for (A) $N_z = 5$ and (B) $N_z = 10$.

TABLE 1 RMS errors of the magnetotelluric responses for the half-space resistivity model.

Frequency (Hz)	TM mode		TE mode	
	Apparent resistivity	Phase	Apparent resistivity	Phase
0.01	7.73e-9	3.11e-8	7.71e-9	3.09e-8
0.1	1.83e-6	1.74e-7	1.81e-6	1.72e-7
1	1.69e-4	5.32e-5	1.62e-4	5.24e-5
10	1.26e-2	1.25e-2	1.21e-2	1.22e-2
100	0.39	1.42	0.36	1.39

3.2 Spectral basis functions

Its spectral accuracy characterizes the spectral element, i.e., the numerical error depends on the order of the basis functions (Lee and Liu, 2005). We choose Gauss-Lobatto-Legendre (GLL) element discretization for the magnetotelluric forward problem. The N th-order GLL basis functions in a one-dimensional reference element $\xi \in [-1, 1]$ can be expressed by

$$\phi_i(\xi) = \frac{1}{N(N+1)L_N(\xi_i)} \frac{\xi^2 - 1}{\xi - \xi_i} L'_N(\xi) \quad (19)$$

for $i = 1, 2, \dots, N + 1$, where $L_N(\xi)$ is the N th-order Legendre polynomial and $L'_N(\xi)$ is its derivative. On a reference element with $\xi, \eta \in [-1, 1] \times [-1, 1]$, the two-dimensional basis function can be written as

$$N_{ij}(\xi, \eta) = \phi_i(\xi)\phi_j(\eta) \quad (20)$$

For example, if order $p = 4$, there are 25 basis functions to the interpolation nodes. Figure 2 shows two-dimensional basis functions of the 4th order in part, and four of the nodal basis functions corresponding to $N_{12}(\xi, \eta) = \phi_1(\xi)\phi_2(\eta)$, $N_{22}(\xi, \eta) = \phi_2(\xi)\phi_2(\eta)$, $N_{34}(\xi, \eta) = \phi_3(\xi)\phi_4(\eta)$, and $N_{45}(\xi, \eta) = \phi_4(\xi)\phi_5(\eta)$ are represented.

3.3 Spectral element equation

In the spectral element method, a physical sub-element needs to be mapped into a reference parent element and the element coefficient matrix can be achieved in the reference element. Figure 3 shows a mapping example of a two-dimensional spectral element (y, z -coordinate and the normalized $\xi, \eta \in [-1, 1] \times [-1, 1]$ reference coordinate).

The derivatives and the volume in the (y, z)-coordinate system in Eq. 17 can be transformed to the (ξ, η)-coordinate system as follows:

$$dydz = \begin{vmatrix} \frac{\partial y}{\partial \xi} & \frac{\partial z}{\partial \xi} \\ \frac{\partial y}{\partial \eta} & \frac{\partial z}{\partial \eta} \end{vmatrix} d\xi d\eta = |J| d\xi d\eta \quad (21)$$

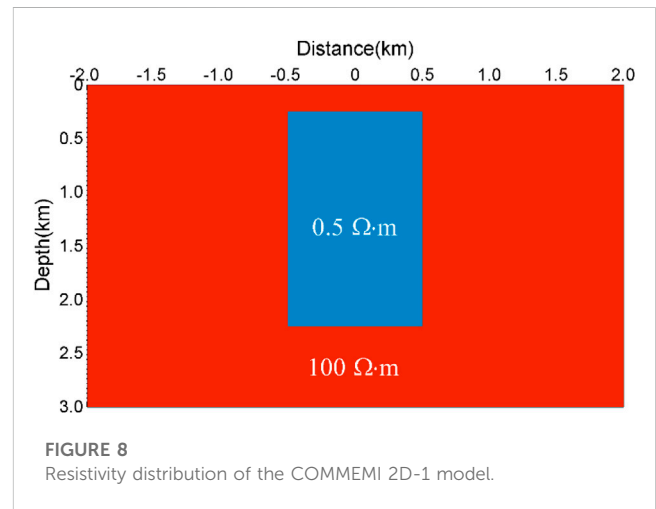


FIGURE 8 Resistivity distribution of the COMMEMI 2D-1 model.

where J is the Jacobian matrix.

The first-term integral in Eq. 17 is

$$\iint_{e2} \frac{1}{2} \tau \left[\left(\frac{\partial u}{\partial y} \right)^2 + \left(\frac{\partial u}{\partial z} \right)^2 \right] dydz = \frac{1}{2} \mathbf{u}_e^T \mathbf{K}_{1e} \mathbf{u}_e \quad (22)$$

where

$$\mathbf{K}_{1e} = \iint_e \left[\left(\frac{\partial u}{\partial y} \right)^2 + \left(\frac{\partial u}{\partial z} \right)^2 \right] dydz = \int_{-1}^1 \int_{-1}^1 \tau \left(\frac{\partial N_i}{\partial \xi} \frac{\partial \xi}{\partial y} \right) \left(\frac{\partial N_j}{\partial \xi} \frac{\partial \xi}{\partial y} \right) |J| d\xi d\eta + \int_{-1}^1 \int_{-1}^1 \tau \left(\frac{\partial N_i}{\partial \eta} \frac{\partial \eta}{\partial z} \right) \left(\frac{\partial N_j}{\partial \eta} \frac{\partial \eta}{\partial z} \right) |J| d\xi d\eta$$

The second-term integral in Eq. 17 is

$$\iint_{e2} \frac{1}{2} \lambda u^2 dydz = \frac{1}{2} \mathbf{u}_e^T \mathbf{K}_{2e} \mathbf{u}_e \quad (23)$$

where $\mathbf{K}_{2e} = \iint_e \lambda u^2 dydz = \int_{-1}^1 \int_{-1}^1 \lambda N_i N_j |J| d\xi d\eta$.

The third-term integral in Eq. 17 is

$$\int_{CD2} \frac{1}{2} \tau k u^2 dl = \frac{1}{2} \mathbf{u}_e^T \mathbf{K}_{3e} \mathbf{u}_e \quad (24)$$

where \mathbf{K}_{3e} can be obtained with a one-dimensional line integral.

Considering the Dirichlet boundary condition at $z = z_{\min}$, we can derive the linear equations with the spectral element approach to build the two-dimensional magnetotelluric forward modeling:

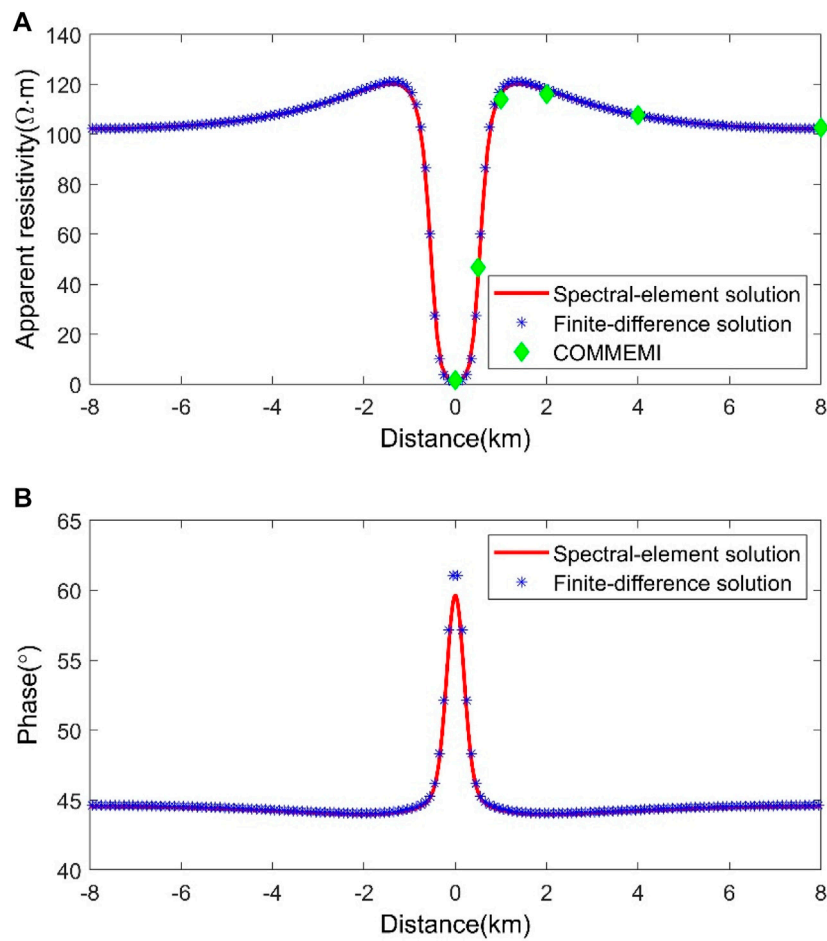


FIGURE 9 Comparison of numerical results for the COMMEMI 2D-1 model in the TM mode. (A) Apparent resistivities and (B) phases.

$$K u = p \tag{25}$$

where $K = \sum_{i=1}^{N_e} K_{1e} - \sum_{i=1}^{N_e} K_{2e} + \sum_{i=1}^{N_e} K_{3e}$ is the coefficient matrix containing conductivity parameters σ , and N_e is the number of all elements. The right-side vector p is interrelated to the Dirichlet boundary conditions. The coefficient matrix K is a sparse, positive-defined, symmetric matrix. Figure 4 shows the sparse elements' distribution of the coefficient matrix for a 3×3 grid with the 4th polynomial order (just for illustration purposes). We use the biconjugate gradient-stabilized algorithm (van der Vorst, 1992; Chen et al., 2002), preconditioned with incomplete LU factorization (Pan et al., 2022), for our forward problem.

After obtaining E_x , the corresponding magnetic field component H_y can be solved by Eq. 4 for the TE mode. Since we acquired H_x , the corresponding electric component E_y can be solved by Eq. 7 for the TM mode. Then, we can obtain the two-dimensional impedance tensor from

$$\begin{bmatrix} E_x \\ E_y \end{bmatrix} = \begin{bmatrix} 0 & Z_{xy} \\ Z_{yx} & 0 \end{bmatrix} \begin{bmatrix} H_x \\ H_y \end{bmatrix} \tag{26}$$

The impedance can be used to calculate apparent resistivities

$$\rho_a^{xy} = \frac{1}{\omega\mu} |Z_{xy}|^2, \rho_a^{yx} = \frac{1}{\omega\mu} |Z_{yx}|^2 \tag{27}$$

and impedance phases

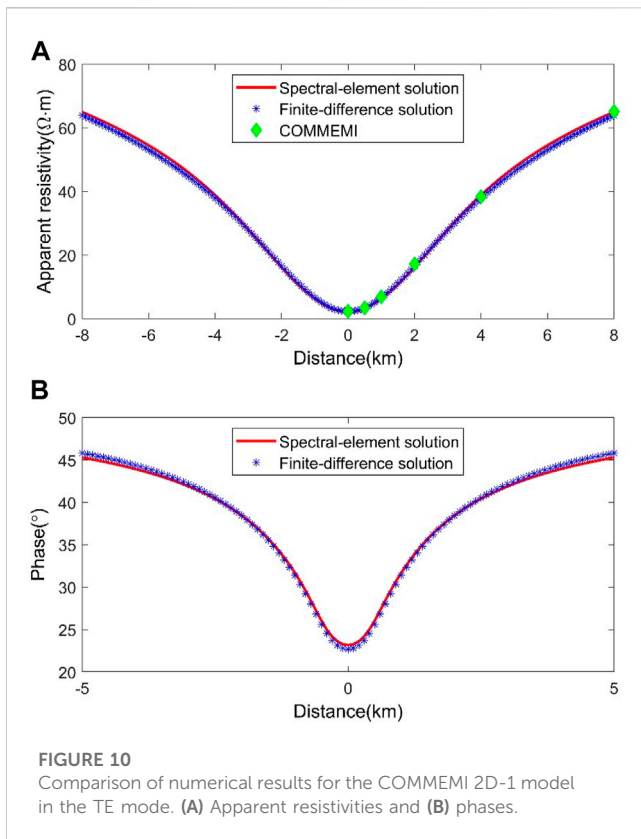
$$\phi^{xy} = \arctan \frac{\text{Im}[Z_{xy}]}{\text{Re}[Z_{xy}]}, \phi^{yx} = \arctan \frac{\text{Im}[Z_{yx}]}{\text{Re}[Z_{yx}]} \tag{28}$$

4 Accuracy of the method

For all the spectral element numerical approaches, the numerical solution of the boundary value problem depends on two parameters: (1) the size of each spectral element and (2) the interpolating polynomial order. To verify our spectral element method numerically, we consider the Dirichlet boundary for a Helmholtz equation

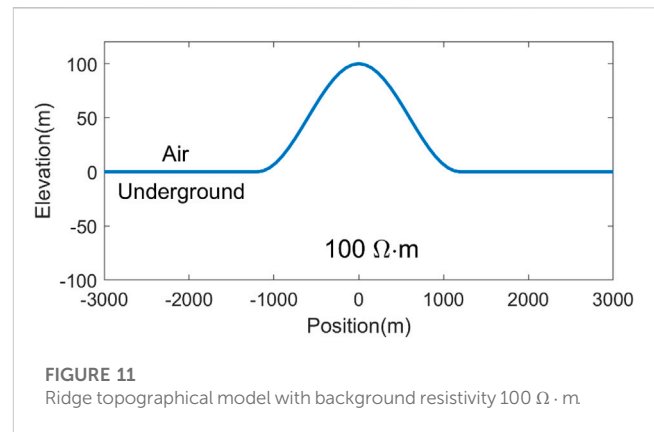
$$\nabla^2 u - u = 3 \tag{29}$$

with the exact solution



$$u_e(x, y) = \sum_{m=1,3,\dots}^{\infty} \sum_{n=1,3,\dots}^{\infty} -\frac{48}{(1 + \pi^2 m^2 + \pi^2 n^2)} \frac{1}{mn\pi^2} \sin(n\pi x) \sin(m\pi y) \quad (30)$$

The physical domain $\Omega = [0, 1] \times [0, 1]$ is discretized using a uniform mesh with 5×5 elements. Figure 5 shows the spectral element solutions obtained using different interpolating polynomial



orders. The maximum absolute errors of spectral element solutions for 2, 3, and 4th polynomial orders are $1.06E-4$, $2.89E-5$, and $7.84E-6$, respectively. The numerical results computed by our spectral element approach are generally consistent with the series solutions.

5 Model studies and discussion

5.1 Homogeneous half-space

We developed a half-space resistivity model to test the high-accuracy benchmark of our spectral element scheme. The half-space resistivity is designed as $10 \Omega \cdot m$ and the computational domain is set as $20 \text{ km} \times 4 \text{ km}$. During numerical simulation, each spectral element includes 4 GLL points in the y -direction and z -direction, as shown in Figure 6. In addition, we assume that only one measuring point is located on the ground, marked by a green triangle. The numerical magnetic field H_x is simulated at $f = 10 \text{ Hz}$.

We set the number of elements in the horizontal direction to 10 (i.e., $N_y = 10$), while the number of elements in the depth direction is designed to 5 and 10, respectively (i.e., $N_z = 10$ and 5). Figure 7

TABLE 2 Apparent resistivities simulated by the spectral element code compared to the COMMEMI results.

	0 m	500 m	1,000 m	2,000 m	4,000 m
ρ_c (T M)					
SEM, $p=1$	1.34	41.49	120.21	117.38	108.20
SEM, $p=2$	1.44	44.56	114.84	115.57	107.23
SEM, $p=3$	1.48	45.76	114.64	116.07	107.40
SEM, $p=4$	1.51	46.02	114.25	116.37	107.81
COMMEMI	1.60 ± 0.27	46.70 ± 3.64	114.01 ± 3.69	116.11 ± 2.67	107.62 ± 2.25
ρ_a (TE)					
SEM, $p=1$	2.27	3.20	6.33	16.20	37.89
SEM, $p=2$	2.28	3.29	6.60	16.59	38.83
SEM, $p=3$	2.30	3.34	6.71	17.06	38.26
SEM, $p=4$	2.30	3.35	6.76	17.12	38.29
COMMEMI	2.31 ± 0.12	3.39 ± 0.36	6.86 ± 0.30	17.19 ± 1.09	38.35 ± 1.96

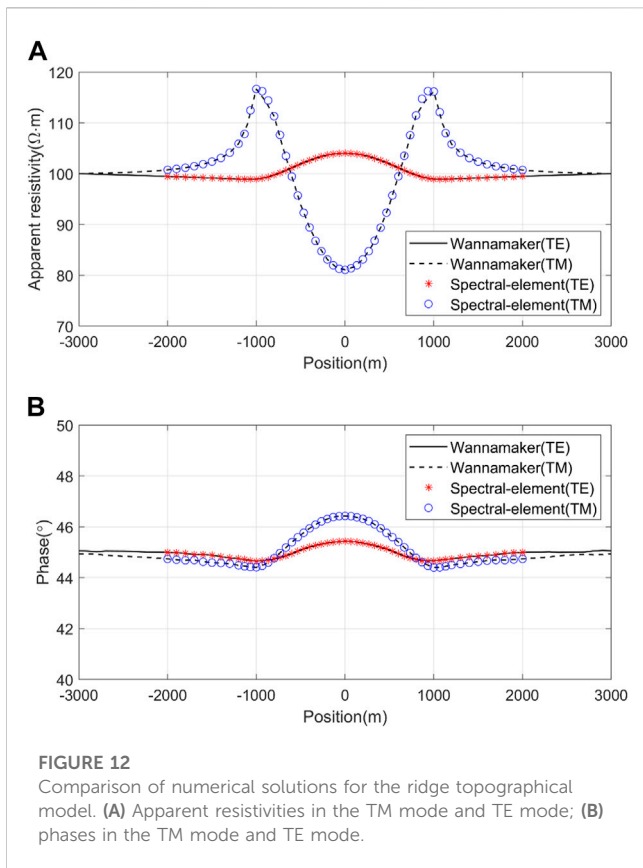


FIGURE 12
Comparison of numerical solutions for the ridge topographical model. (A) Apparent resistivities in the TM mode and TE mode; (B) phases in the TM mode and TE mode.

shows the numerical solution of the magnetic field H_x for the homogeneous half-space frequency of $f = 10$ Hz. They also offer that the real part and imaginary part of the magnetic field H_x calculated by the spectral element method agree with the analytical solution. This phenomenon also shows the correlation between the number of discrete elements and computational accuracy. Furthermore, it indicates that the number of discrete components does not affect the computational accuracy under high-polynomial order conditions. These results suggest that the spectral element approach can improve the accuracy for the two-dimensional magnetotelluric forward modeling.

To further verify the applicability of our spectral element approach, we increase the number of elements in horizontal and depth directions to 20. We then calculated the magnetotelluric response, including apparent resistivity and phase, at $f = 0.1, 1.1, 10, 10,$ and 100 Hz frequencies in the TM mode and TE mode. The computing time of our code is about 1.6 s for each frequency. The apparent resistivity for each frequency is identical to the true resistivity $10 \Omega \cdot m$, and the phase was equal to 45° . The RMS errors of the magnetotelluric responses are given in Table 1. It is clear that the RMS error is proportional to the frequency, with the minimum error at $f = 0.01$ Hz and the maximum error at $f = 100$ Hz. In general, the RMS error value falls within the frequency band that we set, which is also the acceptable error range. The results show that our spectral element approach has high computational accuracy.

5.2 COMMEMI 2D-1 model

We conducted a numerical experiment to compare with the finite difference method. This numerical experiment coincides with the COMMEMI 2D-1 example (Zhdanov et al., 1997), which can test the accuracy and reliability of the spectral element forward algorithm. The COMMEMI 2D-1 model is shown in Figure 8. A symmetrical, rectangular, low-resistivity body is inserted in a homogeneous conductive half-space. The rectangular anomaly body has a width of 1,000 m, a length of 2,000 m, and a burial depth of 250 m from the ground surface. The resistivity of the anomaly is set as $= 0.5 \Omega \cdot m$, and the half-space resistivity is designed as $\rho = 100 \Omega \cdot m$. The frequency we applied in the next two experiments was $f = 0.1$ Hz.

First, we simulated the numerical solutions for the COMMEMI 2D-1 model using the spectral element algorithm and the finite difference method (Tong et al., 2018). In this example, the uniform meshes of the model for the whole calculation area are set to $\Delta y \times \Delta z = 100m \times 50m$. For spectral element numerical modeling, each spectral element includes two GLL points in the y -direction and z -direction, and has nine points for each element. The numerical apparent resistivities and phases in the TM mode are shown in Figure 9. The results show that the numerical results calculated by the spectral element method match well with those of

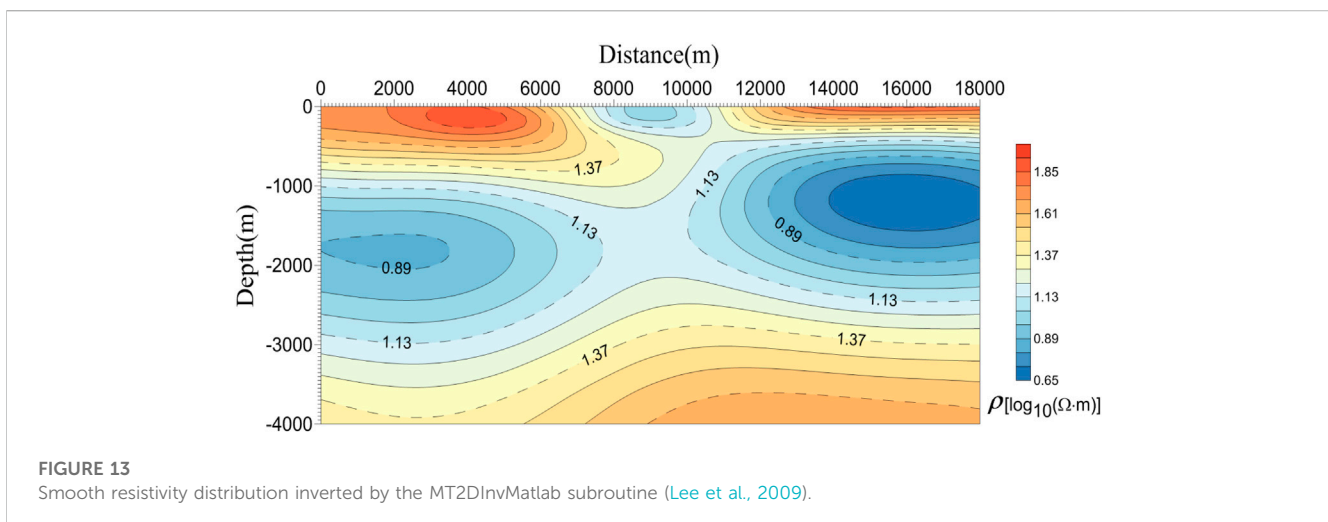
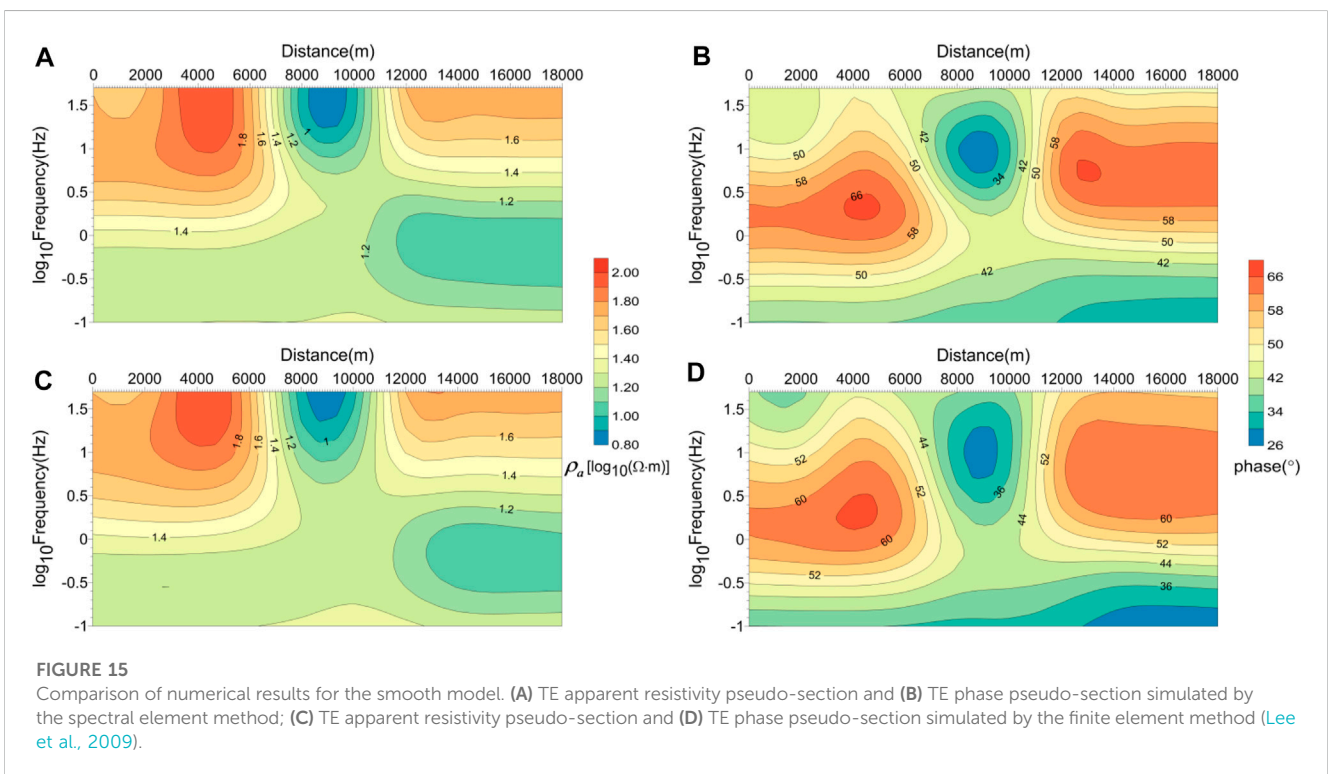
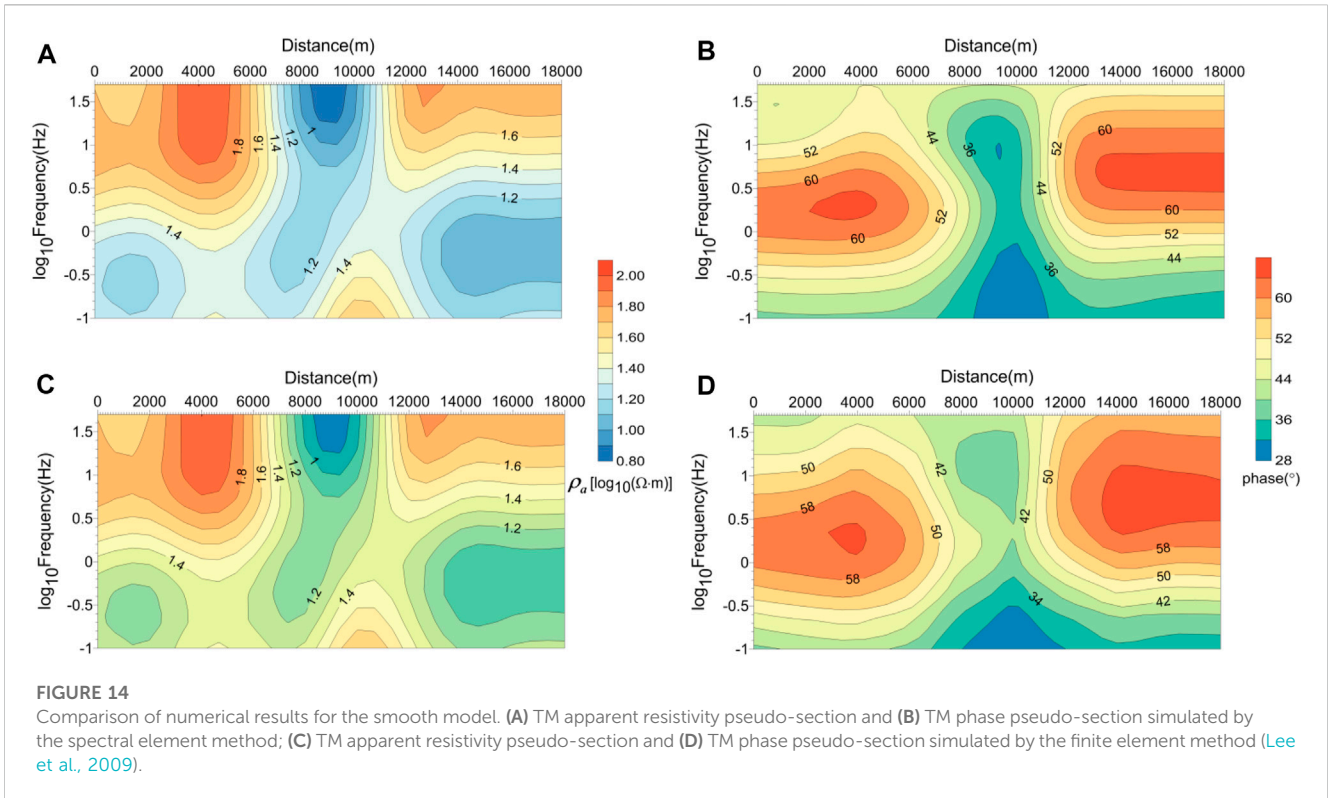


FIGURE 13
Smooth resistivity distribution inverted by the MT2DInvMatlab subroutine (Lee et al., 2009).



the finite difference method. Compared to finite difference results, the spectral element method shows a clear and continuous downward smoothness in TM mode calculations. The numerical results for the TE mode are shown in Figure 10. These results also matched well for the numerical magnetotelluric responses in the TE

mode. The computing time of the COMMEMI 2D-1 model is about 0.5 s for the finite difference algorithm and about 1.8 s for the spectral element algorithm.

We also compare the numerical apparent resistivities calculated by the spectral element scheme and the finite difference approach with the

averaged numerical solutions of the COMMEMI project (Zhdanov et al., 1997), showing that the numerical apparent resistivities of the spectral element scheme agree well with the averaged numerical solutions of the COMMEMI project compared to those measured by the finite difference approach (Figure 9 top; Figure 10 top). It means that the modeling precision of the spectral element scheme is higher than that of the finite difference method in calculating the magnetotelluric responses using the same mesh size.

In the second example, we only simulate the spectral element solutions with different polynomial orders in the COMMEMI locations. In this experiment, we designed a non-uniform grid of the model over the entire computational domain. To make a more precise comparison with the resistivity values published by the committee experiments, in Table 2, we list the standard deviation from Table B.11 (Zhdanov et al., 1997) along with the numerical resistivity values simulated by the spectral element approach. From Table 2, the values produced by the spectral element method match well with the numerical results published in the COMMEMI experiments. The accuracy of the apparent resistivity simulated by the spectral element might depend on the polynomial order.

5.3 Topographical model

To compute the magnetotelluric responses of the two-dimensional undulating terrain, we applied our spectral element code to a ridge topographical model, as shown in Figure 11, which is the same as that used by other researchers (Wannamaker et al., 1986; Liang et al., 2021). The ridge model has a width of 2,400 m with a height of 100 m, and its resistivity value of half-space is $= 100 \Omega \cdot \text{m}$. The calculated magnetotelluric responses obtained by the finite element subroutine (Wannamaker et al., 1986) are the reference for this simulation.

In this study, the non-uniform meshes in the TM mode and TE mode are set as 15×10 and 20×10 , respectively (in which 10 km is the air media and its resistivity is equal to $10^{15} \Omega \cdot \text{m}$), and each spectral element has four GLL points in the y -direction and z -direction. The measurement profile along the atmospheric grounding interface varies from $-2,000$ to $2,000$ m. The frequency to be tested is only 10 Hz. Figure 12 shows the comparison of the finite element results from Wannamaker et al. (1986) and our spectral element forward code, and the results match well. The maximum relative apparent resistivity error between the two forward schemes is equal to 0.15% in the TM mode and 0.07% in the TE mode, respectively. The maximum relative phase error is equal to 0.04% in the TM mode and 0.05% in the TE mode, respectively. As shown in Figure 12A, the topographic resistivity distortion of the TE mode is smaller than that of the TM mode.

5.4 Smooth resistivity model

In this numerical example, a smooth resistivity model is set to $18 \text{ km} \times 4 \text{ km}$, as shown in Figure 13. We calculate the response of a two-dimensional magnetotelluric model with a smooth resistivity distribution. The least-square iterative algorithm calculated the inversion of the resistivity distribution for this model with the MT2DInvMatlab subroutine (Lee et al., 2009) for a fault model tested by Sasaki (1989).

We chose nine frequencies to test this model, which are 0.1, 0.2, 0.5, 1.0, 2.0, 5.0, 10.0, 20.0, and 50.0 Hz (Lee et al., 2009). The computational domain was set as $200 \text{ km} \times 100 \text{ km}$, and the resistivity value for the extended region was designed as $50 \Omega \cdot \text{m}$. We chose four GLL points for each element in the y -direction and z -direction, and 25 points per element. Figures 14, 15 show the pseudo-sections of the apparent resistivity and phase for this smooth model in the TM mode and the TE mode. By comparing the spectral element results and the finite element results, we found that the accuracy of the two ways is almost the same, and the results agree well.

6 Conclusion

The spectral element method combined with the GLL point interpolating scheme has been developed for the first time to solve the two-dimensional magnetotelluric forward problem. We presented the spectral element formulas and implemented this algorithm. Compared with the finite difference scheme and the finite element technique, our spectral element approach requires fewer elements and produces accurate results. In the first investigation, we apply the spectral element strategy on a simple half-space geo-electric model to test its high accuracy. We presented the comparison results of the finite difference algorithm and the spectral element algorithm for the COMMEMI 2D-1 model. The accuracy of our spectral element method is better than that of the finite difference approach. We compare the numerical results from Wannamaker et al. (1986) and our spectral element scheme for a ridge topographical model, and they agree well. These results demonstrate the effectiveness and flexibility of the spectral element forward algorithm. We also applied the spectral element method to a model with a smooth resistivity structure and compared the simulation results with those of the finite element code (Lee et al., 2009). This shows that the calculation results of the spectral element algorithm are as smooth and accurate as those of the finite element method. These measurements and comparative results suggest that the spectral element method can provide another effective scheme for the two-dimensional magnetotelluric forward problem.

Data availability statement

The raw data supporting the conclusion of this article will be made available by the authors, without undue reservation.

Author contributions

All authors participated in editing and reviewing the manuscript. XT derived the linear equation system of the spectral element approach and developed the numerical simulation code. YS performed the numerical experiments and result analysis. BZ plotted some of the figures. All authors read and agreed to the submitted version of the manuscript.

Funding

This research work was partly supported by the National Natural Science Foundation of China under grants 42274083 and 41974049, and partly by the Hunan National Natural Science Foundation under Grant 2023JJ30411.

Acknowledgments

The authors would like to thank Syed Muzyan Shahzad, who modified the whole paper for English writing and gave excellent suggestions to improve the writing quality. They would also like to thank Dawei Gao for checking the numerical results of the paper. Last but not least, they thank reviewers and editors for their helpful suggestions and for improving the manuscript.

References

- Avdeeva, A., Avdeev, D., and Jegen, M. (2012). Detecting a salt dome overhang with magnetotellurics: 3D inversion methodology and synthetic model studies. *Geophysics* 77 (4), 251–263. doi:10.1190/geo2011-0167.1
- Azeez, K. K., Patro, P. K., Harinarayana, T., and Sarma, S. V. (2017). Magnetotelluric imaging across the tectonic structures in the eastern segment of the Central Indian Tectonic Zone: Preserved imprints of polyphase tectonics and evidence for suture status of the Tan Shear. *Precambrian Res.* 298, 325–340. doi:10.1016/j.precamres.2017.06.018
- Barcelona, H., Favetto, A., Peri, V., Pomposiello, C., and Ungarelli, C. (2013). The potential of audio magnetotellurics in the study of geothermal fields: A case study from the northern segment of the La candelaria range, northwestern Argentina. *J. Appl. Geophys.* 88 (1), 83–93. doi:10.1016/j.jappgeo.2012.10.004
- Benjamin, M. L., Unsworth, J. H., Jeremy, P. R., Jean, M. L., and Legault, J. M. (2018). 3D joint inversion of magnetotelluric and airborne tipper data: A case study from the morrisson porphyry Cu–Au–Mo deposit, British Columbia, Canada. *Geophys. Prospect.* 66 (2), 397–421. doi:10.1111/1365-2478.12554
- Bihlo, A., Farquharson, C. G., Haynes, R. D., and Loredó-Ostí, J. C. (2017). Probabilistic domain decomposition for the solution of the two-dimensional magnetotelluric problem. *Comput. Geosci.* 21 (1), 117–129. doi:10.1007/s10596-016-9598-8
- Chave, A. D., and Jones, A. G. (2012). *The magnetotelluric method: Theory and practice*. Cambridge: Cambridge University Press.
- Chen, J., Haber, E., and Oldenburg, D. W. (2002). Three-dimensional numerical modeling and inversion of magnetometric resistivity data. *Geophys. J. Int.* 149 (3), 679–697. doi:10.1046/j.1365-246X.2002.01688.x
- deGroot-Hedlin, C. (2006). Finite-difference modeling of magnetotelluric fields: Error estimates for uniform and nonuniform grids. *Geophysics* 71 (3), 97–106. doi:10.1190/1.2195991
- deGroot-Hedlin, N. C., and Constable, S. (1990). Occam's inversion generates smooth, two-dimensional models from magnetotelluric data. *Geophysics* 55 (12), 1613–1624. doi:10.1190/1.1442813
- Du, H. K., Ren, Z. Y., and Tang, J. T. (2016). A finite-volume approach for 2D magnetotellurics modeling with arbitrary topographies. *Studia Geophys. Geod.* 60 (2), 332–347. doi:10.1007/s11200-014-1041-9
- Franke, A., Börner, R. U., and Spitzer, K. (2007). Adaptive unstructured grid finite element simulation of two-dimensional magnetotelluric fields for arbitrary surface and seafloor topography. *Geophys. J. Int.* 171 (1), 71–86. doi:10.1111/j.1365-246X.2007.03481.x
- Gharti, H. N., Tromp, J., and Zampini, S. (2018). Spectral-infinite-element simulations of gravity anomalies. *Geophys. J. Int.* 215 (2), 1098–1117. doi:10.1093/gji/ggy324
- Guo, R., Li, M., Yang, F., Xu, S., and Abubakar, A. (2020). Application of supervised descent method for 2D magnetotelluric data inversion. *Geophysics* 85 (4), 53–65. doi:10.1190/geo2019-0409.1
- Guo, Z. Q., Egbert, G. D., and Wei, W. B. (2018). Modular implementation of magnetotelluric 2D forward modeling with general anisotropy. *Comput. Geosciences* 118, 27–38. doi:10.1016/j.cageo.2018.05.004
- Huang, X., Farquharson, C. G., Yin, C., Yan, L., Cao, X., and Zhang, B. (2021). A 3D forward-modeling approach for airborne electromagnetic data using a modified spectral-element method. *Geophysics* 86 (5), 343–354. doi:10.1190/geo2020-0004.1
- Huang, X., Yin, C., Farquharson, C. G., Cao, X., Zhang, B., Huang, W., et al. (2019). Spectral-element method with arbitrary hexahedron meshes for time-domain 3D airborne electromagnetic forward modeling. *Geophysics* 84 (1), 37–46. doi:10.1190/geo2018-0231.1
- Jiang, W., Duan, J., Doublier, M., Clark, A., Schofield, A., Brodie, R., et al. (2022). Application of multiscale magnetotelluric data to mineral exploration: An example from the east tennant region, northern Australia. *Geophys. J. Int.* 229 (2), 1628–1645. doi:10.1093/gji/ggac029
- Kalscheuer, T., Juhonjuntti, N., and Vaittinen, K. (2018). Two-dimensional magnetotelluric modelling of ore deposits: Improvements in model constraints by inclusion of borehole measurements. *Surv. Geophys.* 39 (3), 467–507. doi:10.1007/s10712-017-9454-y
- Kelbert, A., Meqbel, N., Egbert, G. D., and Tandon, K. (2014). ModEM: A modular system for inversion of electromagnetic geophysical data. *Comput. Geosciences* 66, 40–53. doi:10.1016/j.cageo.2014.01.010
- Key, K., and Weiss, C. (2006). Adaptive finite-element modeling using unstructured grids: The 2D magnetotelluric example. *Geophysics* 71 (6), 291–299. doi:10.1190/1.2348091
- Komatitsch, D., and Tromp, J. (1999). Introduction to the spectral element method for three-dimensional seismic wave propagation. *Geophys. J. Int.* 139 (3), 806–822. doi:10.1046/j.1365-246x.1999.00967.x
- Kumar, K., Gupta, P. K., and Niwas, S. (2011). Efficient two-dimensional magnetotellurics modelling using implicitly restarted Lanczos method. *J. Earth Syst. Sci.* 120 (4), 595–604. doi:10.1007/s12040-011-0093-2
- Lee, J. H., and Liu, Q. H. (2005). An efficient 3-D spectral-element method for Schrödinger equation in nanodevice simulation. *IEEE Trans. Computer-Aided Des. Integr. Circuits Syst.* 24 (2), 1848–1858. doi:10.1109/TCAD.2005.852675
- Lee, S. K., Kim, H. J., Song, Y., and Lee, C. K. (2009). MT2Dinvmatlab—A program in MATLAB and FORTRAN for two-dimensional magnetotelluric inversion. *Comput. Geosciences* 35 (8), 1722–1734. doi:10.1016/j.cageo.2008.10.010
- Liang, J. W., Tong, D. F., Tan, F., Jiao, Y. Y., and Yan, C. W. (2021). Two-Dimensional magnetotelluric modelling based on the numerical manifold method. *Eng. Analysis Bound. Elem.* 124 (1), 87–97. doi:10.1016/j.enganabound.2020.12.011
- Liao, X., Shi, Z., Zhang, Z., Yan, Q., and Liu, P. (2022). 2D inversion of magnetotelluric data using deep learning technology. *Acta Geophys.* 70, 1047–1060. doi:10.1007/s11600-022-00773-z
- Luo, Y., Tromp, J., Denel, B., and Calandra, H. (2013). 3D coupled acoustic-elastic migration with topography and bathymetry based on spectral-element and adjoint methods. *Geophysics* 78 (4), 193–202. doi:10.1190/geo2012-0462.1
- Lyu, C., Capdeville, Y., and Zhao, L. (2020). Efficiency of the spectral element method with very high polynomial degree to solve the elastic wave equation. *Geophysics* 85 (1), 33–43. doi:10.1190/geo2019-0087.1
- Martin, R., Chevrot, S., Komatitsch, D., Seoane, L., Spangenberg, H., Wang, Y., et al. (2017). A high-order 3D spectral-element method for the forward modelling and inversion of gravimetric data - application to the Western Pyrenees. *Geophys. J. Int.* 209 (1), ggx010–424. doi:10.1093/gji/ggx010
- Nagarajuna, D., Rao, C. K., Pavankumar, G., Kumar, A., and Manglik, A. (2021). Magnetotelluric evidence for an Archaean – proterozoic lithospheric assemblage within the Cambay rift basin, Western India, and its role in channeling of plume-derived fluids within the basin. *Tectonophysics* 818, 229064. doi:10.1016/j.tecto.2021.229064

Conflict of interest

The authors declare that the research was conducted in the absence of any commercial or financial relationships that could be construed as a potential conflict of interest.

Publisher's note

All claims expressed in this article are solely those of the authors and do not necessarily represent those of their affiliated organizations, or those of the publisher, the editors, and the reviewers. Any product that may be evaluated in this article, or claim that may be made by its manufacturer, is not guaranteed or endorsed by the publisher.

- Pan, K., Wang, J., Hu, S., Ren, Z., Cui, T., Guo, R., et al. (2022). An efficient cascading multigrid solver for 3-D magnetotelluric forward modelling problems using potentials. *Geophys. J. Int.* 230 (3), 1834–1851. doi:10.1093/gji/ggac152
- Patera, A. T. (1984). A spectral element method for fluid dynamics: Laminar flow in a channel expansion. *J. Comput. Phys.* 54 (3), 468–488. doi:10.1016/0021-9991(84)90128-1
- Patro, P. K. (2017). Magnetotelluric studies for hydrocarbon and geothermal resources: Examples from the Asian region. *Surv. Geophys.* 38, 1005–1041. doi:10.1007/s10712-017-9439-x
- Pek, J., and Verner, T. (1997). Finite-difference modelling of magnetotelluric fields in two-dimensional anisotropic media. *Geophys. J. Int.* 128 (3), 505–521. doi:10.1111/j.1365-246X.1997.tb05314.x
- Pozrikidis, C. (2014). *Introduction to finite and spectral element methods using MATLAB*. New York: Chapman and Hall Press.
- Rao, K. P., and Babu, G. A. (2006). EMOD2D—A program in C++ for finite difference modeling of magnetotelluric TM mode responses over 2D Earth. *Comput. Geosciences* 32 (9), 1499–1511. doi:10.1016/j.cageo.2006.02.017
- Rodi, W., and Mackie, R. L. (2001). Nonlinear conjugate gradients algorithm for 2-D magnetotelluric inversion. *Geophysics* 66 (1), 174–187. doi:10.1190/1.1444893
- Sarakorn, W. (2017). 2-D magnetotelluric modeling using finite element method incorporating unstructured quadrilateral elements. *J. Appl. Geophys.* 139, 16–24. doi:10.1016/j.jappgeo.2017.02.005
- Sarakorn, W., and Vachirienchai, C. (2018). Hybrid finite difference–finite element method to incorporate topography and bathymetry for two-dimensional magnetotelluric modeling. *Earth, Planets Space* 70 (1), 103. doi:10.1186/s40623-018-0876-7
- Sasaki, Y. (1989). Two-dimensional joint inversion of magnetotelluric and dipole-dipole resistivity data. *Geophysics* 54 (2), 254–262. doi:10.1190/1.1442649
- Seriani, G., and Oliveira, S. P. (2008). Dispersion analysis of spectral element methods for elastic wave propagation. *Wave Motion* 45 (8), 729–744. doi:10.1016/j.wavemoti.2007.11.007
- Siripunvaraporn, W., and Egbert, G. D. (2007). Data space conjugate gradient inversion for 2-D magnetotelluric data. *Geophys. J. Int.* 170 (3), 986–994. doi:10.1111/j.1365-246X.2007.03478.x
- Tarek, A. H., Mohamed, A. Z., Gad, E. Q., Hossam, M., Samah, E., and Yasuhiro, F. (2023). Deep heat source detection using the magnetotelluric method and geothermal assessment of the Farafra Oasis, Western Desert, Egypt. *Geothermics* 109, 102648. doi:10.1016/j.geothermics.2023.102648
- Tong, X., Guo, Y., and Xie, W. (2018). Finite difference algorithm on non-uniform meshes for modeling 2D magnetotelluric responses. *Algorithms* 11 (2), 203–217. doi:10.3390/a11120203
- Tong, X., Sun, Y., and Guo, R. (2020). A Chebyshev pseudo-spectral approach for simulating magnetotelluric TM-mode responses on 2D structures. *J. Appl. Geophys.* 179, 104085. doi:10.1016/j.jappgeo.2020.104085
- Trinh, R. T., Brossier, R., Metiver, L., Tavaré, L., and Virieux, J. (2019). Efficient time-domain 3D elastic and viscoelastic full-waveform inversion using a spectral-element method on flexible Cartesian-based mesh. *Geophysics* 84 (1), 61–83. doi:10.1190/geo2018-0059.1
- Unsworth, M. (2010). Magnetotelluric studies of active continent-continent collisions. *Surv. Geophys.* 31 (2), 137–161. doi:10.1007/s10712-009-9086-y
- van der Vorst, H. A. (1992). Bi-CGSTAB: A fast and smoothly converging variant of Bi-cg for the solution of nonsymmetric linear systems. *SIAM J. Sci. Comput.* 13 (2), 631–644. doi:10.1137/0913035
- Wang, N., Tang, J., Ren, Z., Xiao, X., and Huang, X. (2019). Two-dimensional magnetotelluric anisotropic forward modeling using finite-volume method. *Chin. J. Geophys.* 62 (10), 3912–3922. doi:10.6038/cjg2019M0498
- Wannamaker, P. E., Stodt, J. A., and Rijo, L. (1987). A stable finite element solution for two-dimensional magnetotelluric modelling. *Geophys. J. Int.* 88 (1), 277–296. doi:10.1111/j.1365-246X.1987.tb01380.x
- Wannamaker, P. E., Stodt, J. A., and Rijo, L. (1986). Two-dimensional topographic responses in magnetotellurics modeled using finite elements. *Geophysics* 51 (11), 2131–2144. doi:10.1190/1.1442065
- Weiss, M., Kalscheuer, T., and Ren, Z. (2023). Spectral element method for 3-D controlled-source electromagnetic forward modelling using unstructured hexahedral meshes. *Geophys. J. Int.* 232 (2), 1427–1454. doi:10.1093/gji/ggac358
- Wittke, J., and Tezkan, B. (2014). Meshfree magnetotelluric modelling. *Geophys. J. Int.* 198 (2), 1255–1268. doi:10.1093/gji/ggu207
- Wittke, J., and Tezkan, B. (2021). Two-dimensional meshless modelling and TE-mode inversion of magnetotelluric data. *Geophys. J. Int.* 226 (2), 1250–1261. doi:10.1093/gji/ggab147
- Xu, J., Tang, J., and Xiao, X. (2022). A hybrid spectral element-infinite element approach for 3D controlled-source electromagnetic modeling. *J. Appl. Geophys.* 200, 104619. doi:10.1016/j.jappgeo.2022.104619
- Xu, S., and Zhou, H. (1997). Modelling the 2D terrain effect on MT by the boundary-element method. *Geophys. Prospect.* 45 (6), 931–943. doi:10.1046/j.1365-2478.1997.610301.x
- Yao, H., Ren, Z., Chen, H., Tang, J., Li, Y., and Liu, X. (2021). Two-dimensional magnetotelluric finite element modeling by a hybrid Helmholtz-curl formulae system. *J. Comput. Phys.* 443, 110533. doi:10.1016/j.jcp.2021.110533
- Yin, C., Liu, L., Liu, Y., Zhang, B., Qiu, C., and Huang, X. (2019). 3D frequency-domain airborne EM forward modelling using spectral element method with Gauss-Lobatto-Chebyshev polynomials. *Explor. Geophys.* 50 (5), 461–471. doi:10.1080/08123985.2019.1614162
- Zhang, K., Wei, W., Lu, Q., Dong, H., and Li, Y. (2014). Theoretical assessment of 3-D magnetotelluric method for oil and gas exploration: Synthetic examples. *J. Appl. Geophys.* 106, 23–36. doi:10.1016/j.jappgeo.2014.04.003
- Zhdanov, M. S., Varentsov, I. M., Weaver, J. T., Golubev, N. G., and Krylov, V. A. (1997). Methods for modelling electromagnetic fields results from COMMEMI—the international project on the comparison of modelling methods for electromagnetic induction. *J. Appl. Geophys.* 37 (3-4), 133–271. doi:10.1016/S0926-9851(97)00013-X
- Zhou, Y., Shi, L., Liu, N., Zhu, C., Liu, H., and Liu, Q. (2016). Spectral element method and domain decomposition for low-frequency subsurface EM simulation. *IEEE Geoscience Remote Sens. Lett.* 13 (4), 550–554. doi:10.1109/LGRS.2016.2524558
- Zhu, J., Yin, C., Liu, Y., Liu, Y., Liu, L., Yang, Z., et al. (2020). 3-D dc resistivity modelling based on spectral element method with unstructured tetrahedral grids. *Geophys. J. Int.* 220 (3), 1748–1761. doi:10.1093/gji/ggz534
- Zou, P., and Cheng, J. (2018). Pseudo-spectral method using rotated staggered grid for elastic wave propagation in 3D arbitrary anisotropic media. *Geophys. Prospect.* 66 (1), 47–61. doi:10.1111/1365-2478.12543